

AD-A158 929

ACTA AERONAUTICA ET ASTRONAUTICA SINICA (SELECTED
ARTICLES)(U) FOREIGN TECHNOLOGY DIV WRIGHT-PATTERSON
AFB OH R ZHOU ET AL. 23 JUL 85 FTD-ID(R5)T-0206-85

1/1

UNCLASSIFIED

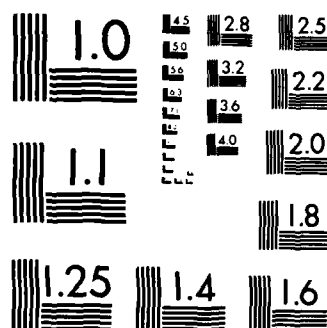
F/G 20/4

NL

END

FILMED

DTIC



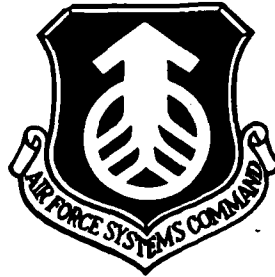
MICROCOPY RESOLUTION TEST CHART
NATIONAL BUREAU OF STANDARDS-1963-A

2

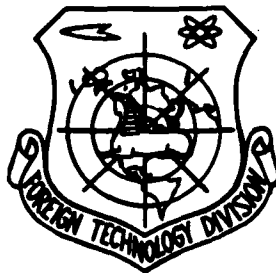
FTD-ID(RS)T-0206-85

AD-A158 929

FOREIGN TECHNOLOGY DIVISION



ACTA AERONAUTICA ET ASTRONAUTICA SINICA
(Selected Articles)



Approved for public release;
distribution unlimited.

DTIC FILE COPY



EDITED TRANSLATION

FTD-ID(RS)T-0206-85

23 July 1985

MICROFICHE NR: FTD-85-C-000566

ACTA AERONAUTICA ET ASTRONAUTICA SINICA (Selected Articles)

English pages: 43

Source: Hangkong Xuebao, Vol. 5, Nr. 3,
September 1984, pp. 261-266; 288-295;
333-337

Country of origin: China

Translated by: FLS, INC.

F33657-85-D-2079

Requester: FTD/TQTA

Approved for public release; distribution unlimited.



A-1

THIS TRANSLATION IS A RENDITION OF THE ORIGINAL FOREIGN TEXT WITHOUT ANY ANALYTICAL OR EDITORIAL COMMENT. STATEMENTS OR THEORIES ADVOCATED OR IMPLIED ARE THOSE OF THE SOURCE AND DO NOT NECESSARILY REFLECT THE POSITION OR OPINION OF THE FOREIGN TECHNOLOGY DIVISION.

PREPARED BY:

TRANSLATION DIVISION
FOREIGN TECHNOLOGY DIVISION
WP-AFB, OHIO.

TABLE OF CONTENTS

Calculation of Aerodynamic Characteristics on Wing-Tip Mounted Winglets and Experimental Verification; by Zhou Renliang.....	1
Study on Algorithms for Prediction of Solid Propellant Rocket Motor Performance; by Wang Xin and Zhang Zhongqin.....	13
Turbulent Vortices and Bionics in Turbojet, by Ning Huang and Gao Ge.....	30

GRAPHICS DISCLAIMER

All figures, graphics, tables, equations, etc. merged into this translation were extracted from the best quality copy available.

CALCULATION OF AERODYNAMIC CHARACTERISTICS ON WING-TIP MOUNTED WINGLETS AND EXPERIMENTAL VERIFICATION

Zhou Renliang

Nanjing Institute of Aeronautics and Astronautics

Received 1 July 1983

The finite basic solution method is employed in this paper for calculating the subsonic lift and drag characteristics of a back-swept wing with wing-tip mounted winglets. Calculations have also been performed on its pitching moment and wing root bending moment. Through calculations of various wing-tip mounted winglet configurations, the general rules of wing-tip mounted winglet aerodynamic characteristics have been analyzed. A comparison between calculated results and experimental data reveals, that this method can satisfy the needs for the preliminary design and configuration selection of a wing-tip mounted winglet.

Symbols

C_{s_0}	drag coefficient at zero lift	$m_s^{C_s}$	$\frac{dm_s}{dC_s}$
C_l	lift coefficient	$m_s^{C_l}$	$\frac{dm_s}{dC_l}$
m_s	bending moment coefficient at wing root	δ	$\left(\frac{C_{si}}{C_s^2}\right) \left(\frac{1}{\pi A}\right)$ induced drag factor
m_s	pitching moment coefficient	K_{\max}	$\left(\frac{C_l}{C_s}\right)_{\max}$ maximum ratio of lift to drag
α	angle of attack	\bar{p}	pressure coefficient
C_s	$\frac{dC_l}{d\alpha}$	\bar{x}	relative value of chordwise distance

1. Preface

A few papers concerning theoretical calculations of wing-tip mounted winglets have been seen in foreign journals in recent years. Yet, basically no experimental verifications have been conducted. Therefore, the extent of their practical applications cannot be determined. At present, in China and abroad, research of configuration selections for wing-tip mounted winglets generally employs experimental methods. This is both expensive and time consuming. Moreover, only a few types of winglet are used in experiments and their configurations are relatively simple. Based on the existing data, the general rules of wing-tip mounted winglet aerodynamic characteristics are still inconclusive. This paper presents a theoretical calculation method utilizing the finite basic solution method to calculate the subsonic lift and drag characteristics of a back-swept wing with wing-tip mounted winglets. Calculations have also been performed for the pitching moment and the wing root bending moment. Thereby the general rules

of the wing-tip mounted winglet, geometrical dimensions, and the winglet rake angle, etc. can be studied. In order to verify the applicabilities of this calculation method, force and pressure experiments were conducted on some of the calculated examples. The calculated results basically conform well with the experimental data; therefore, this calculating method has practical significance in the preliminary design and configuration selection of the wing-tip mounted winglets.

II. Calculation Method and Results

In the finite basic solution method employed in the paper, the equal deflection angle method is used to plot the spanwise grid and to determine the locations of the spanwise control points; for chordwise, the equal partial method determines the grid. Grids are laid out on the wing and wing-tip mounted winglets. A compressible horseshoe vortex is laid out on each grid and the attached vortex is placed at the $1/4$ chord line in the grid. Two free vortices are extended along the streamline to infinity. Chordwise locations of the control points are set at the $3/4$ chord line of the grid. The flow boundary conditions at each control point of the main wing and wing-tip mounted winglets are satisfied. A combined flow field method is employed for calculating induced drag [1, 2].

The two-dimensional sizes of back-swept main wing and winglet calculated in this paper are shown in Fig. 1.

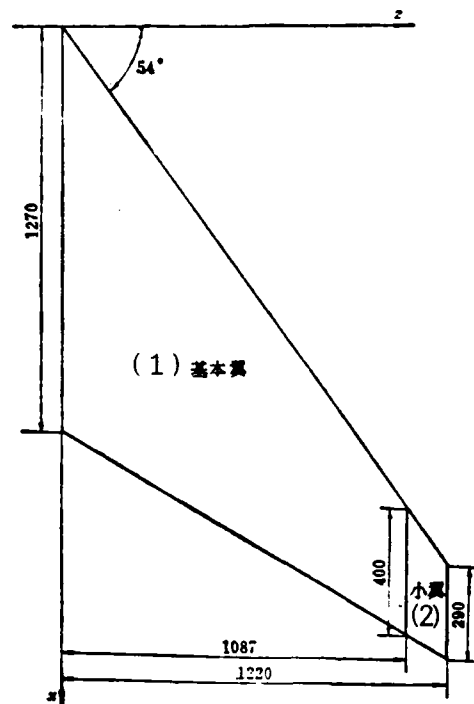


Fig. 1. The two-dimensional sizes of swept main wing and winglet.

Key: (1) The main wing; (2) The winglet.

During the calculation, wing and winglet are divided into 5 columns in the chordwise direction; and into a total of 10 rows in the spanwise direction with 7 rows occupied by the main wing and 3 rows by the winglet. If the winglet is cut in the chordwise direction, it is divided into five strips. Each strip may possess a different angle of rake so that various different winglet arrangements can be formed. A total of 14 winglet arrangements have been calculated in the paper. The 14 winglet arrangements and their three-dimensional schematic diagrams are shown in Fig. 2.




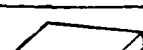
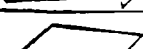


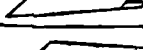
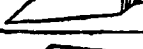
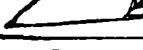
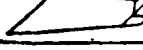



①	(x, x, x, x, x)	
②	(90, 90, 90, 90, 90)	
③	(75, 75, 75, 75, 75)	
④	(-75, -75, -75, -75, -75)	
⑤	(0, 0, 0, 0, 0)	
⑥	(54, 54, 75, 75, 75)	
⑦	(0, 20, 40, 60, 80)	
⑧	(80, 60, 40, 20, 0)	
⑨	(0, 60, 20, 30, 40)	
⑩	(0, 0, 75, 75, 75)	
⑪	(0, 0, 55, 65, 75)	
⑫	(0, 60, 40, 20, 0)	
⑬	(0, 45, 60, 15, 0)	
⑭	(0, 50, 10, 30, 20)	

Fig. 2. The three-dimensional figures of winglet arrangements.

The degrees of rake angle of the 5-strip winglets are given in the parentheses in Fig. 2. The order of the rake angles is from the leading to the trailing edges. The wing-chord plane is the datum plane for angle measuring. Upward rake is positive and downward rake is negative. Arrangement 1 (X, X, X, X, X) shown in Fig. 2 is a main wing without mounted winglet. In order to facilitate the comparison of aerodynamic characteristics for each winglet arrangement, the area, the span to chord ratio, the mean aerodynamic chord and the span length of the main wing are used as the reference area and reference lengths during calculations of aerodynamic coefficients for various arrangements. The aerodynamic characteristics for 14 winglet arrangements obtained from calculations are listed in Table 1.

Table 1. The result of calculation

(1) 方 案	C_y^a	$m_{\dot{C}_y}$	$m_{\dot{C}_y}$	δ
①	0.0465	-0.5189	-0.9783	1.0050
②	0.0493	-0.5454	-1.0116	0.8755
③	0.0500	-0.5529	-1.0207	0.8599
④	0.0500	-0.5529	-1.0207	0.8599
⑤	0.0526	-0.5797	-1.0532	0.7967
⑥	0.0512	-0.5648	-1.0349	0.8173
⑦	0.0539	-0.5923	-1.0693	0.7413
⑧	0.0535	-0.5884	-1.0700	0.7661
⑨	0.0537	-0.5902	-1.0680	0.7409
⑩	0.0528	-0.5809	-1.0547	0.7591
⑪	0.0535	-0.5875	-1.0634	0.7513
⑫	0.0536	-0.5893	-1.0670	0.7414
⑬	0.0536	-0.5891	-1.0662	0.7440
⑭	0.0537	-0.5908	-1.0686	0.7451

Key: (1) Arrangement.

Comparing the data of various winglet arrangements, the following observations can be made:

1) No matter what kind of winglet is added to the main wing, its C_y^a value is always somewhat higher than that of main wing arrangement 1. The induced drag characteristics are somewhat improved as the δ value is decreased. However, values of its $m_{\dot{C}_y}$ and $m_{\dot{C}_y}$ are also somewhat increased as value of C_y^a is increased.

2) It can be seen from the trends of arrangements 2~5 that, the smaller the rake angle of the one-piece winglet is, the larger C_y^a is and the smaller δ is. The aerodynamics coefficients for arrangements 3 and 4 are identical, which shows that, regardless of whether the winglet rake is positive or negative, the aerodynamic characteristics of a one-piece winglet are basically identical so long as the degrees of rake angle remain the same.

3) For the two-piece winglet arrangement 6, the aerodynamic performances of C_y and δ are not as good as that of the wing elongating winglet arrangement 5. However, it is better than the one-piece winglet arrangements 2~4.

4) For a multiple-piece winglet arrangement (rake angles of the 5 winglet strips are all different), its C_y and δ are better than other winglet arrangements. The values of C_y and δ are similar for the various multiple-winglet arrangements. Therefore, from the standpoint of increasing the lift and decreasing the induced drag, a multiple-winglet arrangement is a better selected arrangement.

The above four concluding remarks are consistent with conclusions for rectangular wing in reference [1], which illustrates that, regardless of a rectangular or a back-swept wing, the trends of aerodynamic characteristics changes are identical after a wing tip winglet is mounted on it.

III. Experimental Method and Results

The experiments described in this paper were performed in a NH-2 low-speed wind tunnel at Nanjing Institute of Aeronautics and Astronautics. The wind speed of experiments was 40 m/s. The main wing model used was a wooden semi-mould model. Holes for pressure tappings were drilled on the wooden main wing. The main wing wing-tip was mounted with winglets. Winglets were made of aluminum plate of 1.5 mm in thickness. No pressure tapping holes were drilled on the winglets. Thus, for that model, measurements of pressure distributions were made only on the main wing. In order to save both experimental time and expenditure, only winglet arrangements 1~9 were investigated. Experimental work included force tests and some pressure tests. The angle of attack for all experiments ranged from $4^\circ \sim 24^\circ$. The main characteristics data obtained from force test experiments are listed in Table 2.

Table 2. The result of experiment

(1) 方案	C_y^0	$m_{C_y}^0$	$m_{C_y}^0$	C_{D0}	δ	K_{max}
①	0.0502	-0.4608	-1.0050	0.0079	1.3928	13.1986
②	0.0518	-0.4761	-1.0271	0.0077	1.2928	13.4992
③	0.0526	-0.4833	-1.0257	0.0085	1.2853	13.7652
④	0.0526	-0.4868	-1.0412	0.0088	1.2397	13.7526
⑤	0.0568	-0.5153	-1.0852	0.0086	1.2825	15.1720
⑥	0.0540	-0.4974	-1.0596	0.0091	1.2701	13.1029
⑦	0.0552	-0.5086	-1.0743	0.0097	1.2113	13.2870
⑧	0.0554	-0.5006	-1.0753	0.0097	1.2511	12.9284
⑨	0.0553	-0.5053	-1.0728	0.0096	1.2205	13.2834

Key: (1) Arrangement.

It can be seen from the comparison between data listed in Tables 1 and 2 that the magnitudes of the calculated values for C_y^0 , $m_{C_y}^0$, and $m_{C_y}^0$ are basically similar to those of the experimental data; except that the calculated values of δ are markedly smaller than those of the experimental data. Experimental findings and calculated results of the aerodynamic characteristics for various winglet arrangements are found to be consistent. In other words, the aforementioned four concluding remarks which were derived from calculations have all been verified in the experiments, except for the following two minor discrepancies between the experimental values and the calculated results.

1) The experimental value of δ in winglet arrangement 4 is less than that of winglet arrangement 3.

2) The experimental value of δ in winglet arrangement 6 is less than that of winglet arrangement 5.

Calculations and experiments have all proved that the values of δ for multiple-piece winglet arrangements 7~9 are less than those for 2~6 winglet arrangements. This indicates that the induced drag characteristics of multiple-piece winglets are better

Equations (19)~(21) are further expressed as calculation forms. We have

$$\frac{\partial \rho}{\partial x} = \frac{1}{a^2 - v^2} \left[-\frac{a^2 - v^2}{v} \frac{\partial \rho}{\partial t} - \rho \frac{\partial v}{\partial t} + \frac{1}{v} \frac{\partial p}{\partial t} \right] + \frac{1}{a^2 - v^2} \left[\frac{1}{v} (a^2 - v^2) \varepsilon + \rho \beta - \frac{1}{v} \psi \right] \quad (22)$$

$$\frac{\partial v}{\partial x} = \frac{1}{a^2 - v^2} \left[v \frac{\partial v}{\partial t} - \frac{1}{\rho} \frac{\partial p}{\partial t} \right] + \frac{1}{a^2 - v^2} \left[-v \beta + \frac{1}{\rho} \psi \right] \quad (23)$$

$$\frac{\partial p}{\partial x} = \frac{1}{a^2 - v^2} \left[-\gamma p \frac{\partial v}{\partial t} + v \frac{\partial p}{\partial t} \right] + \frac{1}{a^2 - v^2} (\gamma p \beta - v \psi) \quad (24)$$

At any given time instant, if values of $\partial \rho / \partial t$, $\partial v / \partial t$, and $\partial p / \partial t$ in equations (22)~(24) are known, the above set of equations can be regarded as an ordinary differential equation set with respect to x . The solution can now be obtained by using the Triple-Loop-Iteration Algorithm described above. After the values of ρ , v , and p at all node points in the axial direction are obtained for a certain time instant, they are subtracted by their corresponding values at the previous time instant and then divided by the time interval between the two time instants, thereby the mean change rates for the ρ , v , and p values with respect to time at any node point between those two time instants are calculated. With the mean change rates as the approximation for $\partial \rho / \partial t$, $\partial v / \partial t$, and $\partial p / \partial t$ and substituting them into equations (22)~(24), these equations can then be solved by repeating the aforementioned method. Thus, by repeatedly alternating the calculations with respect to time and space independent variables, the $\partial \rho / \partial t$, $\partial v / \partial t$, and $\partial p / \partial t$ values are corrected through iteration. After a certain accuracy order is achieved the calculations for the next time instant are initiated and the whole process is continued until the rocket motor operation is completed.

By rewriting equations (22)~(24) in a vector form, we have

$$\frac{\partial \vec{u}}{\partial x} = A \frac{\partial \vec{u}}{\partial t} \quad (25)$$

The essence of Time-Space Alternate Algorithm is to transform a set of partial differential equations into a set of ordinary differential equations. With respect to time or space independent variables, a higher order of accuracy for the solution is obtained by using this algorithm. In reference [6], Burstein employed a similar algorithm for solving hyperbolic-type equations and obtained a third order accuracy for both time and space independent variables. The Time-Space Alternate Algorithm employed in this paper not only achieves a fourth order accuracy with respect to space independent variable but also provides a good link between solution methods for the unsteady equations and the quasi-steady equations.

In the Time-Space Alternate Algorithm, ρ , v , and p are selected as dependent variables. First, equations (1) ~ (3) are rearranged as

$$\frac{\partial \rho}{\partial t} + v \frac{\partial \rho}{\partial x} + \rho \frac{\partial v}{\partial x} = \alpha \quad (19)$$

$$\frac{\partial v}{\partial t} + v \frac{\partial v}{\partial x} + \frac{1}{\rho} \frac{\partial p}{\partial x} = \beta \quad (20)$$

$$\frac{\partial p}{\partial t} + \gamma p \frac{\partial v}{\partial x} + v \frac{\partial p}{\partial x} = \psi \quad (21)$$

where

$$\alpha = \frac{1}{A_r} (\rho_r - \rho) q r - \frac{1}{A_r} \rho v \frac{\partial A_r}{\partial x}$$

$$\beta = - \frac{\rho_r v q r}{A_r \rho}$$

$$\psi = \frac{q r}{A_r} \left(\rho_r \gamma R T_b + \frac{\gamma - 1}{2} \rho_r v^2 - p \right) - \frac{\gamma p v}{A_r} \frac{\partial A_r}{\partial x}$$

parameters at time t_n should first be obtained from grain calculation. Within time interval Δt , the thickness Δy_i of the burned-out grains is calculated by the following formula:

$$\Delta y_i = r_i \Delta t$$

where r_i is the average combustion rate within the time interval Δt . This value is dependent upon the combustion rate at time t_n . However, the combustion rate is also affected by all combustion gas parameters and consequently, it is also affected by Δy_i . Therefore, it must be solved for through the successive iteration method. We have employed a single-prediction and multiple-correction approach. Details of the iteration formulae are:

$$r_i^{(0)}(t_n) = r_i(t_{n-1}), \quad (m = 1, 2, \dots)$$

$$r_i^{(n)}(t_n) = \frac{1}{2} [r_i(t_{n-1}) + r_i^{(n-1)}(t_n)], \quad (n = 1, 2, \dots)$$

When employing the Merson Method to conduct numerical integration, it requires grain geometrical parameters at certain points between two node points and also their derivative values with respect to X . These data are obtained by the interpolation of LaGrange quadratic polynomial equation and by the corresponding numerical differential formulae.

3. Time-Space Alternate Algorithm

The governing equations (1)~(4) of a one-dimensional unsteady internal ballistic performance analysis are the first order, linear, hyperbolic partial differential equations. Due to the limitations in the difference method's stability condition, the time increment must be set very small if the characteristic line method is used to solve these equations. For a typical rocket motor, ten thousand or even more iterations are required. This is very inconvenient and sometimes even unacceptable.

After determining boundary conditions of p_0 and m_0 at the motor head, the Merson Method is employed to calculate the initial condition problem of equations (10) and (11). Then, a correction equation is applied to correct the p_0 value in accordance with the exit boundary conditions. For this purpose, the generation rate of the combustion gas \dot{m}_b and the combustion gas exhaust rate \dot{m}_e are given by

$$\begin{aligned}\dot{m}_b &= \dot{m}_i + \dot{m}_A \\ \dot{m}_e &= C_D p_0 A_e\end{aligned}$$

where \dot{m}_A - the generation rate of the combustion gas on the tail-end surface of the grain. The flow from the cross-section at grain exit to the nozzle throat is also considered quasi-steady. Consequently, \dot{m}_e should be equal to \dot{m}_b . After one iteration, if the calculated values of \dot{m}_e and \dot{m}_b are not equal, it indicates improper p_0 guess value and the value has to be corrected. The first correction for p_0 is performed by the following proportional formula:

$$p_0^{(2)} = p_0^{(1)} \dot{m}_b / \dot{m}_e \quad (17)$$

After the number of iteration exceeds two, an interpolation formula can be used for p_0 correction.

Let $\Delta \dot{m} = \dot{m}_e - \dot{m}_b$, thus,

$$\begin{aligned}p_0^{(n)} &= p_0^{(n-1)} + \Delta \dot{m}^{(n-1)} \frac{p_0^{(n-1)} - p_0^{(n-2)}}{\Delta \dot{m}^{(n-2)} - \Delta \dot{m}^{(n-1)}} \\ &\quad (n = 3, 4, \dots)\end{aligned} \quad (18)$$

Iteration is terminated when $\Delta \dot{m}$ is less than a specified value.

When proceeding with the solution at time t_n after the solution at time t_{n-1} has been obtained, the geometrical

The solution method for the set of internal ballistic equations is a kind of boundary condition problem and is not an initial condition problem. Thus, an initialization guess method is employed. First, assuming the guess value of pressure p_0 at the motor head and at time t_0 can be estimated in accordance with the following formulae:

$$p_0 = \left\{ \frac{\rho_r a_1 A_1 a_0}{A_r} \frac{2(\gamma + 1)}{\gamma} \frac{1}{I(\lambda_1)} \right\}^{\frac{1}{1-\gamma}} \quad (12)$$

where

$$I(\lambda_1) = \int_0^{\lambda_1} \frac{4(1-\lambda^2)}{(1+\lambda^2)^2 \left(1 - \frac{\gamma-1}{\gamma+1} \lambda^2\right)^{\frac{\gamma}{\gamma-1}} \epsilon(\lambda)} d\lambda \quad (13)$$

The above λ_1 is determined by

$$J = \frac{A_1}{A_{r1}} = \lambda_1 \left(1 - \frac{\gamma-1}{\gamma+1} \lambda_1^2\right)^{\frac{1}{\gamma-1}} \left(\frac{\gamma+1}{2}\right)^{\frac{1}{\gamma-1}} \quad (14)$$

At time t_1 , the initial guess value of p_0 is taken from the value of p_0 which satisfies continuity at time t_0 . At time t_2 and other later time instants, initial guess values of p_0 are obtained by the following proportion using the p_0 values at two previous time instants; i.e.

$$p_0(t_m) = p_0(t_{m-1}) \frac{p_0(t_{m-1})}{p_0(t_{m-2})}, \quad (m = 2, 3, \dots) \quad (15)$$

At any time instant, the mass flow rate across the cross-section 0 should be equal to the generation rate of combustion gas on the combustion surface at the motor head. Hence,

$$\dot{m}_0 = A_{10} \rho_r a_1 p_0^n \quad (16)$$

If $v \ll a$, $\rho \ll \rho_r$, $\Delta A_r \ll A_r$ (within the residence time of the combustion gas), the operation process of the rocket motor can be considered quasi-steady. The above equations can be simplified as:

$$\frac{d}{dx}(\rho A_r v) = \rho_r r \frac{dA_r}{dx} \quad (5)$$

$$\frac{d}{dx}(\rho v^2 A_r + p A_r) = p \frac{dA_r}{dx} \quad (6)$$

$$\frac{d}{dx} \left[\rho v A_r \left(\frac{v^2}{2} + H \right) \right] = \rho_r r \frac{dA_r}{dx} H_r \quad (7)$$

$$p = \rho R T \quad (8)$$

2. Triple-Loop-Iteration Algorithm

With respect to a one-dimensional quasi-steady, adiabatic flow, energy equation (7) in the above governing equations (5)~(8) can be simplified as

$$c_p T + v^2/2 = c_p T_r \quad (9)$$

Consequently, only the continuity and momentum equations among the governing equations are expressed in differentiated form. If the mass flow rate \dot{m} and the pressure p are selected as the calculating variables, the continuity and momentum equations can be written as follows:

$$\frac{d\dot{m}}{dx} = \rho_r r \frac{dA_r}{dx} \quad (10)$$

$$\frac{dp}{dx} = \frac{1}{A_r(a^2 - v^2)} \left\{ \rho v^2 a^2 \frac{dA_r}{dx} - \rho_r r \frac{dA_r}{dx} v [2a^2 + (\gamma - 1)v^2] \right\} \quad (11)$$

By using the energy equation and equation of state and other well-known equations, all the unknown parameters can be expressed as functions of \dot{m} and p .

internal ballistic calculations are closely related and must not be separated, a general two-dimensional grain calculation method introduced by the author is employed.

II. Triple-Loop-Iteration and Time-Space Alternate Algorithm

1. Rocket motor model and its one-dimensional internal ballistic governing equations

Figure 1 illustrates a selected solid propellant rocket motor.

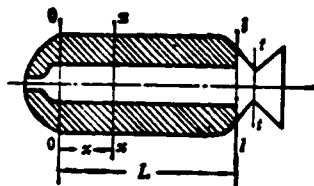


Fig. 1. Schematic of solid propellant rocket motor.

For the simulation of a combustion chamber flow field, the following assumptions have been made: The combustion gas is an ideal gas; the fluid flow through the hollow section of a rocket motor cylinder is a one-dimensional flow; the fluid flow process is a frictionless, adiabatic, non-reactive, homogeneous and gas-phase hydrodynamic process. The projection of the momentum of combustion gas, which is being generated on the combustion surface, on the x-axis is also assumed to be zero. The governing equations of the fluid flow in the rocket motor can be derived as:

$$\frac{\partial}{\partial t}(\rho A_r) + \frac{\partial}{\partial x}(\rho A_r v) = \rho_r r \frac{\partial A_t}{\partial x} \quad (1)$$

$$\frac{\partial}{\partial t}(\rho v A_r) + \frac{\partial}{\partial x}(\rho v^2 A_r + p A_r) = p \frac{\partial A_r}{\partial x} \quad (2)$$

$$\frac{\partial}{\partial t} \left[\rho A_r \left(\frac{v^2}{2} + E \right) \right] + \frac{\partial}{\partial x} \left[\rho v A_r \left(\frac{v^2}{2} + H \right) \right] = \rho_r r \frac{\partial A_t}{\partial x} H_r \quad (3)$$

$$p = \rho R T \quad (4)$$

1. Preface

The main purpose for predicting the solid propellant rocket motor's internal ballistic performance is: based on the original data of rocket motor structures, grain geometrical shapes and dimensions, propellant characteristics, etc. to calculate the distributions, along the length of the combustion chamber, of parameters such as combustion gas pressure p , flow velocity v , density ρ , temperature T , etc. during the motor operation period and their changes with respect to time t .

Throughout the years, there has been great progress in the development of internal ballistic calculation algorithms. The earlier internal ballistic calculation algorithms were established on the simplified bases of zero-dimensional and quasi-steady flows [1]. Later, one-dimensional flow model was employed as the volumetric filling coefficient became larger and the erosion combustion phenomenon became very distinctive. Based on the one-dimensional fluid flow model analysis and further simplifications to the quasi-steady flow, a set of ordinary differential equations is obtained [2~5]. Thus, the Runge-Kutta Method or Merson Method can be applied for solutions [7]. If the flow is one-dimensional and unsteady, the governing equations for the rocket motor flow calculations become a set of first order, linear, hyperbolic partial differential equations. Under these circumstances, a solution can be obtained by the finite-difference and characteristic line methods [8].

Emphasis of this paper is placed on the introduction of a calculation algorithm generally applicable to both quasi-steady equations and unsteady equations; i.e. the Time-Space Alternate Algorithm. The algorithm was developed on the basis of a Triple-Loop-Iteration Algorithm. Since the grain calculations and the

Nomenclature

a	Speed of sound	r	Combustion rate of propellant
a_1	Burning speed coefficient	R	Universal gas constant
a_c	Critical speed of sound	T	Combustion gas temperature
A_c	Combustion area	q	Circumference of combustion
A_m	Combustion surface at entrance to the motor head	T_0	Adiabatic combustion temperature
A_p	Passage area	t	Time
A_n	Nozzle area	v	Combustion gas velocity
C_D	Exhaust gas coefficient	x	Axial coordinate
h	Space increment	γ	Specific heat ratio
H	Enthalpy of combustion gas	λ	Velocity coefficient
H_p	Enthalpy of propellant	ρ	Combustion gas density
\dot{m}	Mass flow rate	ρ_p	Propellant density
n	Pressure index	ϵ	Erosion-consumption ratio
p	Combustion gas pressure	τ	Time increment

Subscripts

0	Cross-sectional area parameter of grain at inlet \emptyset	i	Nozzle parameter
l	Cross-sectional area parameter of grain at exit	s	Stagnation parameter

STUDY ON ALGORITHMS FOR PREDICTION OF SOLID PROPELLANT ROCKET MOTOR PERFORMANCE

Wang Xin and Zhang Zhongqin

Beijing Institute of Aeronautics and Astronautics

Received 17 September 1983

Two algorithms for prediction of solid propellant rocket motor performance are introduced, and the emphasis is placed on the Time-Space Alternate Algorithm. A two-dimensional grain general calculation method introduced by the authors for the calculation of grain is employed. Thus, the method presented in this paper for predicting the internal ballistic performance has the generality of applicabilities. A comprehensive computer program for the above method has been written and applied to calculating the performance of three different solid propellant rocket motors. The calculated results are consistent with the experimental data.

It can be observed from the comparison between the theoretical calculations and experimental data that said theoretical calculating method can be employed to conduct preliminary evaluation of various winglet arrangements, and it has practical significance in the preliminary design and configuration selection of the wing-tip mounted winglets.

References

1. Renliang, Zhou. Calculation of Lift and Drag Characteristics of a Subsonic Wing with Wing-Tip Mounted Winglets. "Astronautica Sinica," 2, 1981.
2. Jiankuang, An. The Locations of Spanwise Controlling Points and Induced Lift Problems for the Calculation of a Subsonic Wing by the Finite Basic Method. "7210 Sinica," 1, 1977.
3. Whitcomb, Richard T. A Design Approach and Selected Wing-Tunnel Results at High Subsonic for Wing-Tip Mounted Winglets. "NASA TND-8260."
4. Padakannaya, Raghuveera. Effect of Wing Tip Configuration on the Strength and Position of a Rolled-up Vortex. "NASA CR 66916."
5. Cary, Mitchell D. A Parametric Analysis of Winglet Effect. "AD/A-034 944."

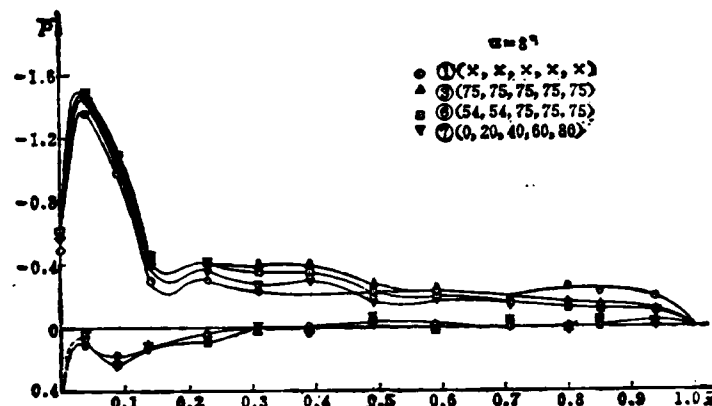


Fig. 4. The experimental curve of pressure distribution.

IV. Concluding Remarks

It is concluded from the above analyses that, the smaller the rake angle of the one-piece winglet is, the larger the C_y of the main wing is and the smaller δ is. However, the length of wing span and the bending moment at the wing root are also increased. Therefore, in foreign countries, winglets with rake angle of about 75° are often selected when an existing transport requires winglet mounting.

The shape of a multiple-piece winglet resembles that of an eagle's wing-tip. It has the best induced drag characteristics. However, the utilization of this type of winglet arrangement on the aircraft often creates certain structural difficulties. Therefore, two-piece winglets are usually mounted on transport aircraft in foreign countries.

Of course, the selection of a better arrangement for mounting wing-tip winglets should be based on specific circumstances and various factors; it can only be determined after a comprehensive analysis of its advantages and disadvantages.

The advantage of lift coefficient for several primary winglets and their relationships can be seen in the experimental curves in Fig. 3 after winglets are mounted on a main wing. It should be pointed out that the relationships shown in Fig. 3 for lift coefficients of various winglet arrangements no longer apply after the angle of attack exceeds 8° . The characteristics of lift to drag ratio also display a similar situation.

The calculations in this paper and reference [1] indicate that, after winglets are mounted, an increase in circulation flux at the main wing outboard region is the main reason for C_y to increase. The experiments of pressure distribution shown in this paper verify that, after the winglets are mounted, the pressure distribution on the inboard region of a main wing is basically the same as that on one without winglets. The cross-sectional pressure distributions at 86.5% main wing span are measured after several primary winglets are mounted and the experimental curves are shown in Fig. 4.

The above experimental curves of pressure distributions show that the pressure distribution on the outboard region of the main wing is markedly increased. This indicates that the conclusions of theoretical calculations are correct.

than those of the one-piece and two-piece winglets. However, values of K_{max} for winglet arrangements 7~9 are often less than those for winglet arrangements 2~6. From the viewpoint of obtaining a larger maximum lift to drag ratio, the multiple-piece winglet is not necessarily a better arrangement. The reason is that the C_{x0} values for multiple-piece winglets are larger (see Table 2) and that, even though their induced drag characteristics are better, the larger C_{x0} values still cause the K_{max} value to decrease.

Figure 3 illustrates several experimental curves of lift coefficient.

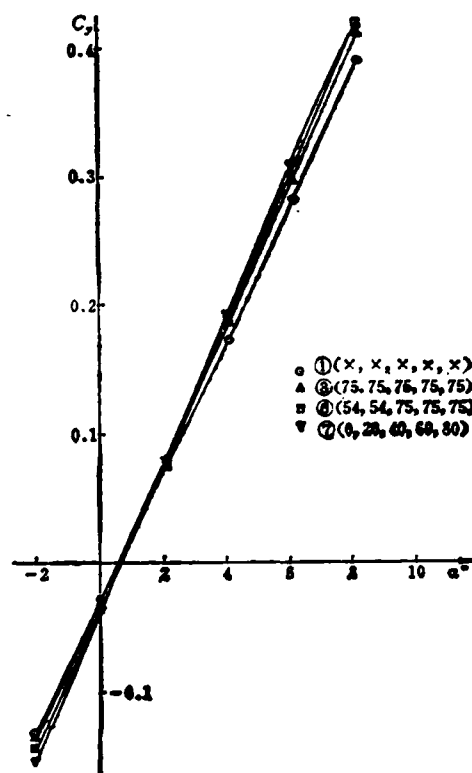


Fig. 3. The experimental curve of lift coefficient.

In order to facilitate the discussion of the stability problem of the difference method, the above equation is generally simplified as:

$$\frac{\partial \vec{u}}{\partial x} = A_0 \frac{\partial \vec{u}}{\partial t} \quad (26)$$

Here, A_0 is a constant matrix.

When the Time-Space Alternate Algorithm is applied for the solution of model equation (26), it is equivalent to applying the difference method.

$$\frac{\vec{u}_{j+1}^{n+1} - \vec{u}_j^{n+1}}{h} = \frac{A_0}{6} \left[\frac{\vec{u}_j^{n+1} - \vec{u}_j^n}{\tau} + 4 \frac{\vec{u}_{j+1/2}^{n+1} - \vec{u}_{j+1/2}^n}{\tau} + \frac{\vec{u}_{j+1}^{n+1} - \vec{u}_{j+1}^n}{\tau} \right] \quad (27)$$

The finite-difference method is, with respect to the model equations, an unconditionally stable scheme. It has been verified through actual calculations that the above conclusion is also applicable to the actual equations.

The Triple-Loop-Iteration Algorithm is employed in consideration of the solutions with respect to the space variable x in the Time-Space Alternate Algorithm. Thus, only the difference between the present method and the quasi-steady equations solution method is introduced here.

The initial conditions required for the Time-Space Alternate Algorithm include initial values of P , v , and p at all node points as well as the initial values of $\partial p / \partial t$, $\partial v / \partial t$, and $\partial p / \partial t$. When the calculations start immediately after the rocket motor ignition process, the above initial conditions can be determined by the results calculated from the ignition process. If, however, the calculations start directly from the steady state period of the rocket motor, we may assume that the flow field inside the combustion chamber reaches steady state instantaneously. Thus, the

values of $\partial \rho / \partial t$, $\partial v / \partial t$, and $\partial p / \partial t$ at all node points can be initially set as zero and the values of P , v , and p at all node points obtained by the Triple-Loop-Iteration Algorithm are used as initial values in the calculations.

Among the boundary conditions at the rocket motor head, the method for determining the p_0 value is the same as the Triple-Loop-Iteration Algorithm. The values of ρ_0 and v_0 , however, are determined by using the following formulae:

$$\rho_0 = p_0 / RT_0$$

$$v_0 = \frac{A_{00} \rho_0 c_0 p_0^m}{\rho_0 A_{r_0}}$$

At time t_n , the values of $\Delta P / \Delta t$, $\Delta v / \Delta t$, and $\Delta p / \Delta t$ between t_{n+1} and t_{n-1} are used as the guess values for $\partial \rho / \partial t$, $\partial v / \partial t$, and $\partial p / \partial t$ at all node points. Having calculated values of P , v , and p at all node points for time t_n , their corrections are subsequently made. The correction formula is

$$\left(\frac{\partial \tilde{u}}{\partial t} \right)_i^{(1+n)} = \frac{\tilde{u}_j^{(n)}(t_n) - \tilde{u}_j(t_{n-1})}{t_n - t_{n-1}}$$

$$(m=1, 2, \dots, n=1, 2, \dots)$$

Corrections can be made repeatedly until the difference between the values of P 's, v 's, and p 's obtained from two successive iterations is less than a specified value.

III. Calculation of Grain

The purpose of the grain calculation is to obtain the grain geometrical parameters required for the instantaneous internal ballistic calculations. For different types of grain calculation, not only the forms of the required grain geometrical parameters are different, the correlation between grain and internal ballistic calculations may also be different. For a zero-dimensional internal ballistic calculation, the required grain geometrical parameters generally correspond with those values of the grain combustion area at a given burned-out thickness. Given this, the grain and the internal ballistic calculations can be performed separately. On the other hand, for the internal ballistic calculation of a one-dimensional, variable cross-sectional tunnel, the required grain geometrical parameters generally correspond with those values of combustion circumference and tunnel area for a partially burned-out thickness at all node points. In view of the existence of erosion burning, the grain and the internal ballistic calculations are closely related and cannot be separated. Thus, calculation must be performed iteratively and alternately.

The method introduced in this paper for the internal ballistic calculation is coordinated with the calculation of the grain. A general two-dimensional grain calculation method [9] is presented by the authors. Based on this method, the solution scheme can be extended to solving, for example, three-dimensional calculation problems of the double-arc, transitionally closed motor head and the unrestrictive combustion tail of the tail-end surface located on the oval portion following the motor.

IV. Sample Calculations and Discussion

A comprehensive computer program for the above mentioned methods was written and applied to the calculation of the performance of three different real rocket motors. For each motor, both the Triple-Loop-Iteration Algorithm and the Time-Space Alternate Algorithm were employed. In examples 1 and 3, since the internal ballistic parameters do not vary significantly with respect to time during the motor operating period, the difference between the results obtained by these two methods is very small. Thus, only the results obtained by the Triple-Loop-Iteration Algorithm are presented. For example 2, respective results obtained by both methods are presented.

Example 1

The grain is bonded to a two-dimensional hollow, cylindrical case of star-shaped interior. The motor head is double-arc, transitionally closed. The motor tail-end surface is located on the oval portion following the motor. The grain combustion is unrestrictive. Calculated results are shown in Fig. 2.

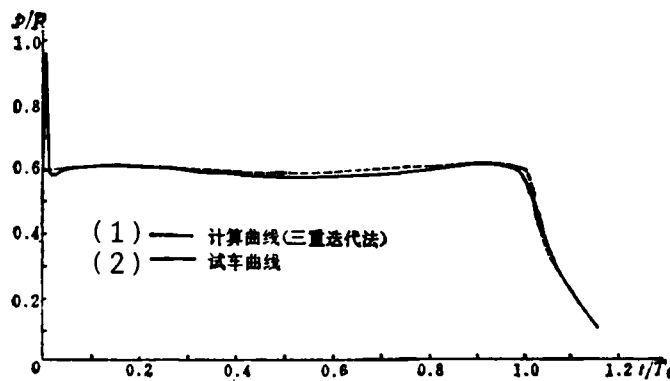


Fig. 2. Pressure vs time for example 1.
Key: (1) Calculated curve (Triple-Loop-Iteration Algorithm); (2) Test curve.

Example 2

The grain is bonded to a two-dimensional hollow, cylindrical case of wheel-shaped interior. Motor head and tail-end surfaces are both located at the cylindrical section following the motor. The grain combustion is unrestrictive. Calculated results are shown in Fig. 3.

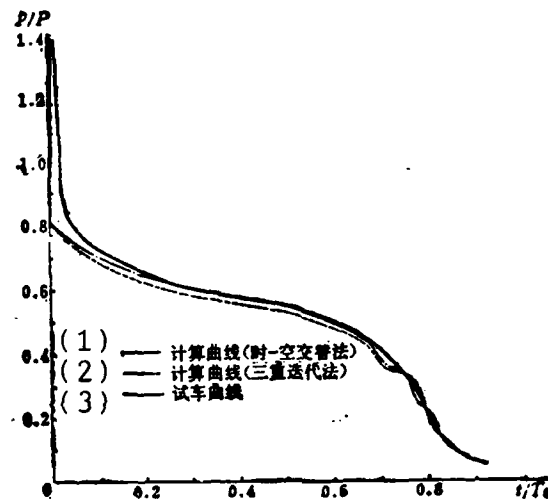


Fig. 3. Pressure vs time for example 2.
Key: 1) Calculated curve (Time-Space Alternate Algorithm); (2) Calculated curve (Triple-Loop-Iteration Algorithm); (3) Test curve.

Example 3

The grain is of a single, tube-shaped configuration with simultaneous combustion on both inner and outer surfaces. Grain combustion on both front- and back-end surfaces are restrictive. Calculated results are shown in Fig. 4.

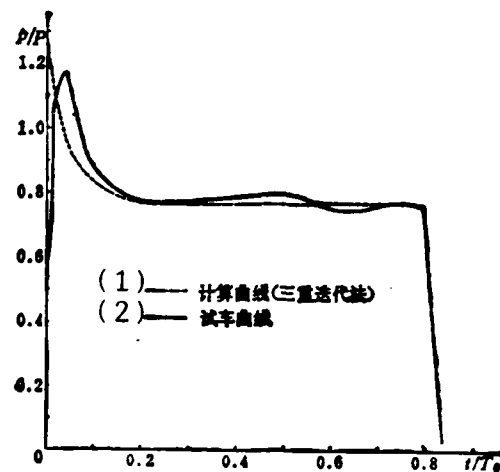


Fig. 4. Pressure vs time for example 3.
Key: (1) Calculated curve (Triple-Loop-Iteration Algorithm); (2) Test curve.

It can be seen from the calculated results that, when the internal ballistic parameters vary considerably with respect to time, significant differences exist between the results obtained from the quasi-steady equations (Triple-Loop-Iteration Algorithm) and from the unsteady equations (Time-Space Alternate Algorithm). The calculation accuracy of the latter is increased by about 1.6% compared to that of the former.

References

1. Burrere, M., Jaumotte, A., Fraeijs de Veubeke, B., and Vandenkerckhove J. Rocket Propulsion. Elsevier Publishing Company, 1960.
2. Sechokoff, A.A.*, translated by Lingshan, Er. Aerodynamics of Solid Propellant Rocket Motors. Defense Industry Publishing Co., 1979.
3. Wieniesky, A.M.*, translated by Jinkang, Yu et al. Solid Propellant Rocket Motors. Defense Industry Publishing Co., 1981.

4. Rayzberg, B.A., Yerokhin, B.T., and Samsorov, K.P. Principles of the Theory of Procedures in Rocket Systems on Solid Fuel. "AD 766567," 1973.
5. Coats, D.E. et al. A Computer Program for the Prediction of Solid Propellant Rocket Motor Performance, Vol. I. "ADA015140," 1975.
6. Burstein, S.Z. and Mirin, A.A. Third Order Difference Methods for Hyperbolic Equations. "J. Comput. Phys.," Vol. 5, No. 3, 1970.
7. Xin, Wang and Zhongqin, Zhang. A Triple-Loop-Iteration Algorithm and Its Computer Program. "Technology Development," No. 4, 1983.
8. Peretz, A., Kuo, K.K., Caveny, L.H., and Summerfield, M. Starting Transient of Solid Propellant Rocket Motors With High Internal Gas Velocities. "AIAA J.," Vol. 11, No. 12, 1973.
9. Xin, Wang and Zhongqin, Zhang. A General Two-Dimensional Grain Calculation Method and Its Computer Program. "Technology Development," No. 3, 1982.

*Translator's note: Transliteration uncertain due to Russian/Chinese/English conversion.

STUDY ON ALGORITHMS FOR PREDICTION OF SOLID PROPELLANT ROCKET MOTOR PERFORMANCE

Wang Xin and Zhang Zhongqin

(Beijing Institute of Aeronautics and Astronautics)

Abstract

Two algorithms for prediction of solid propellant rocket motor performance are introduced. Triple Loop Iteration Algorithm is applied to solution of quasi-steady equations(5)~(8). Its computer program comprises a procedure with three iterative loops. Time-Space Alternate Algorithm can be applied to solving both quasi-steady equations and unsteady equations (22)~(24). If $\partial\rho/\partial t$, $\partial v/\partial t$, $\partial p/\partial t$ in equations (22)~(24) are given, equations (22)~(24) will be reduced to ordinary differential equations. They can be solved by Merson's method. When $\Delta\rho/\Delta t$, $\Delta v/\Delta t$, $\Delta p/\Delta t$ are approximated to $\partial\rho/\partial t$, $\partial v/\partial t$, $\partial p/\partial t$, this algorithm for model equation

$$\frac{\partial \bar{u}}{\partial x} = A_0 \frac{\partial \bar{u}}{\partial \tau}$$

corresponds to the finite difference scheme

$$\frac{\bar{u}_{j+1}^{n+1} - \bar{u}_j^{n+1}}{h} = \frac{A_0}{6} \left[\frac{\bar{u}_j^{n+1} - \bar{u}_j^n}{\tau} + 4 \frac{\bar{u}_{j+1/2}^{n+1} - \bar{u}_{j+1/2}^n}{\tau} + \frac{\bar{u}_{j+1}^{n+1} - \bar{u}_{j+1}^n}{\tau} \right]$$

It is an unconditionally stable scheme.

A general two-dimensional grain calculation method is introduced for calculation of grain. A comprehensive computer program for above mentioned methods has been written and applied to calculating the performance of three different motors. The results of the numerical examples are consistent with the experimental data.

TURBULENT VORTICES AND BIONICS IN TURBOJET

Ning Huang and Gao Ge

Beijing Institute of Aeronautics and Astronautics

Received 2 January 1984

The construction of a modern turbojet is rather complex, but its performance still has many dissatisfactions, viz. great pressure losses along the flow patch, low component efficiencies, proneness of the compressor to stall and surge, frequent occurrence of overheating and oscillations in combustors, difficulty in high-altitude reigniting, and narrow stable operating range. Phenomena of turbulent vortices are discussed in this paper. Newly derived momentum equations for turbulent flow are presented. Some ideas about morphological simulation, which may alleviate the vortex losses and utilize the vortex capabilities, are suggested and thereby produce a few research subjects that are worth further studying.

1. Vortex Occurs Everywhere

Under various flight operating conditions, the occurrence, development, and decay of turbulent vortices are observed everywhere along the flow path of a turbojet from its entrance to exit.

Under subsonic flight condition, the excursion of the flow creates vortices inside the air intake of a turbojet.

Under supersonic flight condition, there are occurrences of boundary layer separation or the laminar flow layers roll up to form turbulent vortex flow field behind the shock waves of the air intake tunnel.

In a compressor, turbulent vortices are created between the clearance of the blade-tips and at the trailing edge of the blade. Between the stator- and rotor-blades, strong vortices are also formed.

In an abrupt expansion type of cylindrical pressure diffuser, stagnation vortices are induced at the edge of the nozzle mouth by the impinging jet fluid. Fluctuations of the fluid flow both upstream and downstream are dampened because of the appearance of a turbulent flow region between the vortices and thereby alleviate interferences.

For a vortex generator or for injector holes of a primary combustion chamber, vortex recirculation region is created at the top of the fire box and thus forms a heat reservoir. This ensures an intensified ignition source and also shortens the flame.

In a gas turbine, vortex trails are installed on both the blade crown and the reinforced rubber between blades. The enthalpy drops can be increased in a single-stage type turbine by controlling vortices at the exhaust of the gas turbine. The number of stages is subsequently reduced. This method has already been used.

A forced-draft combustion chamber uses the vortex recirculation region behind a bluff-body to stabilize flame.

To design turbojet components, we have to study the characteristics of turbulent vortices and their control methods. While vortex turbulent flow consumes energy, loses pressure, reduces efficiency, and causes malfunction, vortices do possess special functions in certain situations.

II. Vortex Characteristics

Turbulent flow can be regarded as a group of small-scale vortices. The vortex characteristics play an important role on turbulent flow characteristics. The turbulent flow is always present whenever there are vortices in the flow field. The types of vortex can be classified as vortex filament, vortex sheet, vortex tube, vortex cluster and eddy. Vortex filaments form a vortex sheet or vortex tube. Cross-sections of vortex ring and vortex cluster are circular vortices. Cross-sections of an eddy are spiral vortices. Vortex filament and vortex tube cannot have free ends. They must either be attached to the interface or connect their two ends in order to form a vortex cluster or an eddy. A vortex sheet cannot exist without a boundary. They must roll up to form an eddy. An eddy may expand to a trumpet shape or contract to a cone shape, and eventually breaks up into turbulent vortex clusters just as eddies in the wing-tip trails or cyclones rising from the ground surface would do. The shapes of vortices

can be changed by flow shifts or by external forces. Their original masses, however, remain unchanged. With respect to its own rotating axis or with respect to the instantaneous center of curvature, a vortex has a rotational angular velocity ω , and a circulation Γ . The circulation of a unit cross-sectional area is called "vorticity" $\Omega = 2\omega$. If the circulation remains constant, the product of the eddy cross-sectional area A and strength of vortex Ω , $\Delta\Omega = \Gamma$, is a constant. For a trumpet-shaped eddy, the end cross-sectional area diverges. Thus, ω becomes too small and then the eddy breaks up. On the other hand, for a cone-shaped eddy, the cross-sectional area of the sharp-end converges. Thus, ω becomes too large. Since the micro-scale gas pockets are being thrown out by centrifugal force, the eddy collapses and disperses into a turbulent flow, thus ω has upper and lower limits.

The circulation of a circular vortex is $\Gamma = \pi r^2 \Omega$. The smaller the value of radius r is, the faster the rotation is. An increase in strengths of a circular vortex would result in the formation of centripetally converging spiral vortices. The combined flow velocity can be increased from subsonic to supersonic. When the limiting flow velocity is reached, a vacuum vortex will appear: An actual vortex core provides low pressure suction, thus creates centripetally converging flow and thereby forms a three-dimensional flow along its axis. The vortex core can be represented by a rotating "solid cylinder core" which induces the surrounding gas to follow the rotation. The tangential velocity at the inner circle is higher than that at the outer one. This is called an active vortex. A mutual induction effect is observed between vortices in this flow field. Therefore, vortex rings have counter-flow, forward-moving velocities.

Shear layers are generated behind the trailing edge of an obstructing bluff-body due to sudden flow velocity change, and a two-dimensional vortex or a three-dimensional vortex ring is formed. Affected by the surrounding gas flow, the tangential velocities inside the vortex is lower than that outside the vortex. Therefore, this is called passive vortex. The stability of the active and passive vortices are different [1].

Observations and experimental studies in recent years reveal that satisfactory explanations, from the standpoint of mechanism, for many characteristics of vortices are still waiting to be discovered. For example, why do tornadoes and eddies at aircraft wing-tips persist for a long time before they decay; why does the top of a typhoon diverge in reverse rotation; why do "negative viscosity" regions appear in the back section of the tail vortices of a nonstreamlined object [2]; although the Ranque-Hilsch effect has already been applied to the cold and hot sublayers of gas flows, the explanations of their mechanisms are still inconclusive [3]. Further understanding of the fundamentals of vortex characteristics, therefore, appears to be a worthwhile research direction.

III. Stability of Vortex

Inside a vortex, flows are moving in separate layers. Diffusive exchanges of momentum, energy, and mass exist when cross-over flow occurs. Moreover, there is also viscous dissipation and centrifugal force flow field. Vortices are pressed and elongated by the surrounding main flow or by the restriction of the solid wall boundary. Between the vortex circumferences of the recirculation flow and the co-current boundary layer streamlines, a narrow, rhombus-shaped vortex tail turbulent region is formed (Fig. 2). This vortex tail turbulent region is densely populated

with small vortex clusters of high vorticity and is very unstable. Local angular velocity ω at the inflection point of the long tail vortex circumference is very high, which often throws gas pockets in the recirculation region into the vortex tail turbulent region causing it to lose stability. If, at the same time, there is external interference caused by strong fluid pressure, the vortex tail will pull the vortices loose, which subsequently collapse to form a downstream turbulent flow field. These are the reasons for instabilities in the vortex recirculation region trailing a regular vortex generator or a V-type stabilizer. The authors believe that "the flame is stable only when the vortex is stable." The stability of vortex is greatly affected by the magnitude of local, instantaneous angular velocity ω of vortex and the length of the vortex tail. From reference [1], the criterion of upper and lower limits for a passive vortex is given by

$$\left| \frac{U'}{4} \right| + \frac{1}{2} \omega, - \left| \frac{g\beta}{U'} \right| \leq \omega \leq \left| \frac{U'}{4} \right| + \frac{1}{2} \omega, \quad (1)$$

where U' gradient of vortex tangential velocity along the radius of curvature r ;

ω_e frequency of external interference wave;

ω local angular velocity of vortex;

g acceleration of a viscous dissipation field; and

β ratio of density gradient along r to the density without interference

Reference [1] also gives a criterion of stability for an active vortex and a spiral vortex. The conditions for intensifying vortex stability can be concluded as: keeping the convergence of vortex tail as short as possible; keeping vortex local ω within the upper and lower limits; attaching itself to a solid boundary to become a resident vortex; having the capability of self-control such that, after interference takes place, the vortex can be recovered back to its original geometrical shape without being detached or being broken up.

IV. Turbulent Vortex Flow Field

In the turbulent vortex flow field, the rolling fluctuations of large and small vortex clusters are of an irregular, randomly-changing process. The Kolmogoroff theory states that large vortex clusters disperse and break up into small vortex clusters. Turbulent kinetic energy is gradually transferred from large vortex clusters to small vortex clusters. Finally, due to viscosity, the turbulent kinetic energy dissipates and results in an energy spectrum. Based on this theory, turbulence model with turbulent kinetic energy k and the turbulent energy dissipation ϵ were developed. The results of calculations for the tail flow of a bluff-body using the k - ϵ model show that the vorticity Ω in the vortex tail turbulent flow region is greatly weakened (Fig. 1). However, the experiments in reference [2] verify that the vorticity Ω in this region is very strong (Fig. 2).

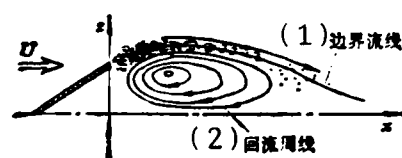


Fig. 1. Weakening vorticity in the vortex tail region (results of calculated by $k-\xi$ model).
Key: (1) Boundary layer streamlines; (2) Recirculation flow circumferences.



Fig. 2. Intensifying vorticity in the vortex tail region (results of experiments) [2].

In regions of high vorticity gradient or pressure sublayers, the dissipation of local turbulent energy is reduced, or even inversed into macroscopic kinetic energy. This is called "energy-inversion" or "negative viscosity" phenomenon. The isotropic turbulence model and statistical methods cannot explain the "intermittency" and the seemingly-irregular yet "orderly-coherent phenomenon" in a turbulent vortex flow. This implies that, under certain circumstances, the appearance of turbulent vortex clusters is not only a pure transport phenomenon but also possesses "Soliton" characteristics [4, 5]. Gao Ge has suggested that the canonical equations of a turbulent vortex flow field should include the "dispersion effects" and combined equations of the K-dV equations with third-order partial derivatives and the Burgers equations:

$$u_t + uu_x - v u_{xx} + \eta u_{xxx} = 0 \quad (2)$$

where v is kinematic viscosity coefficient and η is dispersion coefficient. The "non-isotropic", "orderly-coherent phenomenon", "intermittency", and "energy-inversion" problems of a turbulent flow can be explained after an appropriate and quantitative

construction of the last two terms in equation (2) have been performed. Gao Ge has investigated the relationships between the viscous dissipation and dispersion effects. Momentum equations for turbulent flow are derived as:

$$\frac{\partial u_i}{\partial t} + u_j \frac{\partial u_i}{\partial x_j} = -\frac{1}{\rho} \frac{\partial p}{\partial x_i} + \frac{\partial}{\partial x_j} (v_L + v_T) \left(\frac{\partial u_i}{\partial x_j} + \frac{\partial u_j}{\partial x_i} \right) - 2 \frac{\partial}{\partial x_j} v_T \Omega_{ij} - \text{sign}(u_i) \frac{\partial}{\partial x_j} \eta_T \frac{\partial |\Omega_{ij}|}{\partial x_j} \quad (3)$$

$$\frac{\partial u_i}{\partial t} + u_j \frac{\partial u_i}{\partial x_j} = -\frac{1}{\rho} \frac{\partial p}{\partial x_i} + \frac{\partial}{\partial x_j} (v_L - v_T) \left(\frac{\partial u_i}{\partial x_j} + \frac{\partial u_j}{\partial x_i} \right) - 2 \frac{\partial}{\partial x_j} v_T \Omega_{ij} + \text{sign}(u_i) \frac{\partial}{\partial x_j} \eta_T \frac{\partial |\Omega_{ij}|}{\partial x_j} \quad (4)$$

where v_L , v_T , η_T are the laminar kinematic viscosity, turbulent kinematic viscosity, and turbulent dispersion coefficient, respectively. Vorticity (or degree of circulation) $\Omega_{ij} = \frac{\partial u_j}{\partial x_i} - \frac{\partial u_i}{\partial x_j}$.

The new momentum equations of a turbulent flow are composed jointly of the above equations (3) and (4). Equation (3) is employed for low vorticity cases, while equation (4) is employed for high vorticity cases. Details for determinations of turbulent kinematic viscosity v_T and turbulent dispersion coefficient are the subject of another paper. When the time-averaged vorticity becomes negligibly small, equation (3) is reduced to the Boussinesq viscous turbulent vortex equation; when v_T is very small, the equation is the same as the laminar Navier-Stokes equation. Many turbulence models can be included in the scope of momentum equation (3).

The orderly-coherent phenomena at the boundary layer and turbulent vortex flow problems are successfully solved by using the momentum equation (4). This equation has been applied to the numerical solution for "the energy-inversion phenomena in the turbulent tail vortex flow field of a bluff-body". The calculated results are consistent with the experimental data presented in reference [2]. Calculation is also in good agreement with experiments of "the orderly-coherent phenomena of a horseshoe-shaped pattern in turbulent boundary layers". Reasonable explanation can be provided for many problems such as the non-isotropic turbulence, the Ranque-Hilsch effect of cold and hot layer separation, and the formation of vortex series from the boundary layer separation on a wing model, etc.

It is worthwhile to conduct further theoretical and experimental studies on the dissipation structure and dispersion phenomena of a turbulent vortex flow field. For engineering applications, the above discussions can provide design methods for the prevention of boundary layer separation and thereby improve the performance and efficiency of turbojet components, or reduce the drag on aircraft.

V. Turbulent Vortices and Bionics

The interactions between living things and land shapes versus fluid in the natural environment take various forms. As a fish swims in the water, the vortex trail created by its tail fin movements is almost indiscernible. This is probably due to the absence of boundary layer separation or lack of burden resulted from tail vortex drag. Aquatic plants grow densely in turbulent streams. They grow in long, thin bundles. In order to reduce the impact of water flow, they sway with the current and thereby are able to keep from being uprooted and washed away. With wings wide

stretched, an eagle can glide in the air for a long time. Its wing-tip feathers open up like fingers which weaken wing-tip vortices and thereby reduce drag. Morphological simulation of this feature has been applied to make wing-tip mounted winglets on aircrafts. In the desert, sand dunes are created by gusty winds and their shapes resemble that of a slipper's toe. The front slope of a sand dune is smoothed and streamlined by the wind, with its two arms extending backward and touching each other. Horseshoe-shaped eddies are formed behind the sand dune. This feature matches the stability conditions of a vortex; and therefore, it provides the sand dune with strong resistance to interference.

The natural morphological features are simulated in order to improve turbojet components. Some ideas are first presented as follows:

- 1) In order to simulate the motion of a fish mouth, the air intake and the pressure diffuser throat are manufactured such that they possess automatic expansion and contraction type of structures. With the aid of signal feedback from micro-sensors, the peristaltic, swallowing capability of the air intake tunnel can be automatically controlled and thereby prevent surge.

- 2) In order to simulate the swaying motion of the aquatic plants, air intake tunnel with soft, elastic walls may be manufactured. The wall surface is spray-coated with a film of polytetrafluoroethylene vinyl coating which can reduce frictional force and deaden pressure fluctuations.

3) "The orderly-coherent structure" of a turbulent boundary layer can be utilized to design compressor blade configurations. The range of stable compressor operation and its efficiency can be increased by delaying or preventing the boundary layer from separating and vortices from detaching.

4) In order to simulate an eagle's wings, toughened bladelets are mounted on the blade-tip to reduce vortex drag losses.

5) "Elastic fish tails" are arranged, along the height of blade, on the trailing edge of compressor blades to control vortex detachment and reduce tail vortices.

6) A series of "sand dunes" placed in a circular arrangement can be utilized to replace vortex recirculation region created by vortex generator in the head of a primary combustion chamber. Such a replacement can increase stability and reduce drag.

7) In a forced-draft combustion chamber, the phenomena of horseshoe-shaped eddies being formed behind a "sand dune" can be simulated. This simulation can result in increased combustion stability, oscillation alleviation, drag reduction, and increased combustion efficiency.

References

1. Ge, Gao. On the Research of Local Stability of Vortices. "Journal of Engineering Thermophysics," Vol. 2, No. 4, p. 394. 1981. 6th Symposium ISABE. June, 1983. Paris.
2. Fujii, S., Gomi, M. and Egucei, K. Cold Flow Tests of a Bluff-Body Flame Stabilizer. "J. Fluids Engineering," Vol. 100, Sept. 1978, p. 323.
3. Kurosaka, M. Acoustic Streaming in Swirling Flow and Ranque-Hilsch (Vortex-Tube) Effect. "J. Fluid Mechanics," Vol. 124, 1982, pp. 139-172.
4. Miles, J.W. Solitary Waves. "Ann. Rev. Fluid Mech.," 1980, 12, pp. 11-43.
5. Nishida, Yashushi. Experiments on the Scattering of Ion Acoustic Solitons and Turbulence Formation. "IPPJ-388," May, 1979.

TURBULENT VORTICES AND BIONICS IN TURBOJET

Ning Huang and Gao Ge

(Beijing Institute of Aeronautics and Astronautics)

Abstract

The construction of a modern turbojet is rather complex, but its performance still has many dissatisfactions, viz. great pressure losses along the flow path, low component efficiencies, narrow stable operating range, proneness of the compressor to stall and surge, difficulty in high-altitude relighting, frequent occurrence of overheating and oscillations in combustors. The authors consider that all the above drawbacks are closely related to turbulent vortices, which occur almost everywhere within and around a turbojet. The generation, development and decay of vortices have profound mutual effects with the surrounding flow. In aerodynamic design an endeavour must be made to reduce vortex losses and exploit vortex capabilities. There are some interesting peculiar phenomena in a turbulent vortex flow, such as orderly-coherent flow pattern, intermittency and energy-inversion unconformable to the Kolmogoroff theory of energy spectrum. The traditional isotropic turbulence and statistical treatment cannot explain the above phenomena. The co-author has discovered that viscous dissipation and dispersion effects should be considered simultaneously and Burger's and the K-dV equations have to be mixed up to obtain a canonical equation:

$$u_t + uu_x - \nu u_{xx} + \eta u_{xxx} = 0$$

According to this concept two new momentum equations of turbulent flow are derived:

$$\begin{aligned} \frac{\partial u_i}{\partial t} + u_j \frac{\partial u_i}{\partial x_j} &= -\frac{1}{\rho} \frac{\partial p}{\partial x_i} + \frac{\partial}{\partial x_j} (\nu_L + \nu_T) \left(\frac{\partial u_i}{\partial x_j} + \frac{\partial u_j}{\partial x_i} \right) + 2 \frac{\partial}{\partial x_j} \nu_T \Omega_{ij} \\ &\quad - \text{sign}(u_i) \frac{\partial}{\partial x_j} \eta_T \frac{\partial |\Omega_{ij}|}{\partial x_j} \\ \frac{\partial u_i}{\partial t} + u_j \frac{\partial u_i}{\partial x_j} &= -\frac{1}{\rho} \frac{\partial p}{\partial x_i} + \frac{\partial}{\partial x_j} (\nu_L - \nu_T) \left(\frac{\partial u_i}{\partial x_j} - \frac{\partial u_j}{\partial x_i} \right) - 2 \frac{\partial}{\partial x_j} \nu_T \Omega_{ij} \\ &\quad + \text{sign}(u_i) \frac{\partial}{\partial x_j} \eta_T \frac{\partial |\Omega_{ij}|}{\partial x_j} \end{aligned}$$

Sample computations of a tail vortex flow and an orderly-coherent flow pattern have been performed with success. The authors suggest some ideas about morphological simulation which may alleviate the vortex evils and utilize the vortex characteristics.

END

FILMED

10-85

DTIC